A Deep Learning-Based Real-Time Noise Prediction of Full-Scale Helicopter Rotor

Guowei Zhang — Master's Student
Ilkay Yavrucuk — Professor and Institute Head
Institute of Rotorcraft and Vertical Flight
Technical University of Munich, 80333 Munich, Bavaria, Germany

ABSTRACT

This paper develops a Multilayer Perceptron (MLP) neural network model for predicting full-scale helicopter rotor noise. Given that the neural network model's computational speed is exponentially faster than traditional Ffowcs Williams-Hawkings (FW-H) equation-based solvers, it has the potential to be used in real-time noise prediction. This study aims to assess the capability of the neural network model towards predicting the noise of a full-scale Bo 105 helicopter rotor. The model can be used to predict noise at arbitrary spatial locations at different flight conditions within the design space. A requisite dataset of noise OASPL used to train the model is generated from a FW-H equation solver, PSU-WOPWOP. The rotor acoustic source is obtained by using a mid-fidelity comprehensive analysis code, DYMORE. It was found in the study that, the predicted noise OASPL within the design space is accurate and MLP is able to capture the mathematical relationship between input parameters.

NOTATION

*

Symbols

R Rotor radius, m

N_b Number of blades

Ω Rotor rotation speed, rad/s

p Acoustic pressure, pa

c Speed of sound, m/s

v_n Normal velocity, m/s

ρ_0 Air density, kg/m^3

M Mach number,

r_0 Observer radius, m

ϕ_0 Observer azimuth angle, rad

θ_0 Observer elevation angle, rad

μ Advanced ratio,

β Rotor shaft tilt angle, rad

z Standardized results,

x Original data,

u Mean of original data

s Standard deviation of original data

*

Acronyms

MLP Multilayer Perceptron

FW-H Ffowcs Williams-Hawkings

NN Neural Network

OASPL Overall Sound Pressure Level

CAA Computational Aeroacousitics

CFD Computational Fluid Dynamics

CNN Convlutional Neural Network

VVPM Viscous Vortex Particle Method

INTRODUCTION

Rotorcraft noise is a long-standing issue for public acceptance of rotorcraft and military stealth requirements. Recent developments in Urban Air Mobility (UAM) (Refs. 1–3) have significantly expanded the use and capabilities of rotorcraft. For these UAM vehicles, achieving low noise levels is a primary challenge in their market adoption, as high noise levels are unacceptable to communities. Consequently, the noise footprint of these vehicles has garnered significant attention and is increasingly becoming a subject of research. In this context, noise prediction serves as a powerful tool for assessing the impact of rotorcraft noise on urban environments and for establishing appropriate noise reduction measures.

The aerodynamic noise of rotorcraft is mainly attributed to the rotor. Helicopter rotor noise can be decomposed into several categories, which are the blade self-noise (trailing-edge noise), the rotational noise (thickness and loading noise), the broadband turbulence interaction noise, and the Blade-Vortex Interaction (BVI) noise, where rotational noise is the dominant component of the large full-scale helicopter rotor noise (Ref. 4). Thickness noise is generated from repeated air displacement that is caused by the periodically rotating propeller blades and is dominant in the plane of the rotor so it mainly propagates in the rotor plane and is largely considered as in-plane noise. Loading noise is caused by lift and drag forces that affect the pressure distribution on the blades and it mainly propagates out of the rotor plane and is largely out-of-plane in character. Rotational noise is well-defined at the rotor blade passage frequency (BPF) and has the characteristic of low frequency and high amplitude (Ref. 5). So, this study focuses on the rotor rotational noise prediction.

Generally speaking, rotor noise prediction can be divided into two stages: solving the noise sources and computing acoustic propagation. Most recent methods encompass direct computational aeroacoustics (CAA) and hybrid computational aeroacoustics. Direct computational aeroacoustics computes the noise sources and acoustic propagation through highly accurate computational fluid dynamics (CFD) simulation, leading to massive computation resource consumption. So, it is limited to use only in the final stages of design or benchmark cases (Ref. 6). Hybrid computational aeroacoustics combines the use of unsteady computational fluid dynamics for calculating the properties of acoustic sources with some form of Lighthill's acoustic analogy, such as the FW-H analogy, to calculate the resulting far-field noise radiation. Hybrid acoustic prediction still faces numerous uncertainties associated with the computation of the properties of the acoustic sources, and the coupling of the noise-source computation with the acoustic propagation computation. (Ref. 7).

For acoustic propagation, traditional methods are in the time and frequency domains. Farassat's formulations 1 and 1A, proposed by Farassat (Ref. 8), are widely used for noise prediction in the time domain. Brentner et al. (Ref. 9) presented the unique aspects of the development of an entirely new maneuver noise prediction code called PSU-WOPWOP, which solved the Ffowcs Williams-Hawkings (FW-H) equation (Ref. 10) by Farassat's formulations 1 and 1A to predict noise in the time domain. The frequency domain methods mainly focus on obtaining the frequency domain solutions of ideal sound sources (Ref. 11). Recently, there have been some new methods in the acoustic modal domain. For example, Xu et al. (Ref. 12) proposed a rigid rotor global noise prediction method based on acoustic modes. This acoustic modal domain method has the potential to conduct real-time noise prediction, but its accuracy is not promising. As for traditional time domain and frequency domain methods, a substantial amount of relevant research has proved that they can generate highly promising results. However, their computation costs are too expensive to be used in real-time noise prediction. Thus, the aforementioned time, frequency, and acoustic modal domain methods are not currently suitable for real-time rotorcraft noise prediction.

With the successful development of deep learning technology in recent years, it has also attracted the attention of the rotorcraft community. After being trained with proper datasets, the neural network (NN) can output accurate noise prediction results with negligible computational expense. Therefore, some researchers have integrated traditional noise prediction methods with deep learning methods to achieve fast and accurate noise prediction. Convolutional neural networks (CNN) can learn spatial statistical correlations from structured data, such as images or CFD-simulated flow fields. Alguacil (Ref. 13) proposed a novel multi-scale CNN to predict the next time-step of the acoustic density field given several previous steps. Wiewel (Ref. 14) coupled A type of recurrent neural network (RNN) called Long Short-Term Memory (LSTM) with CNN model the complete space-time evolution of flow fields. Li (Ref. 15) and Thurman (Ref. 16) utilized NN to predict and characterize broadband noise for the hovering rotor. Cur-

Figure 1: Full-scale Bo 105 helicopter rotor in the wind tunnel.

rent deep learning-based noise prediction methods are usually used for rotorcraft design and predict noise at one or several fixed observers. Since the deep learning method can be used to predict and characterize rotor broadband noise, it should also have the potential to rotational noise. Unfortunately, it has not yet been applied to full-scale helicopter rotor rotational noise prediction for arbitrary spatial locations at different flight conditions.

Table 1: Details of Bo 105 rotor.

Rotor type	Hingeless
N_b	4
Airfoil	NACA23012
σ	0.07
R	4.912 m
Ω	44.505 Rad/s

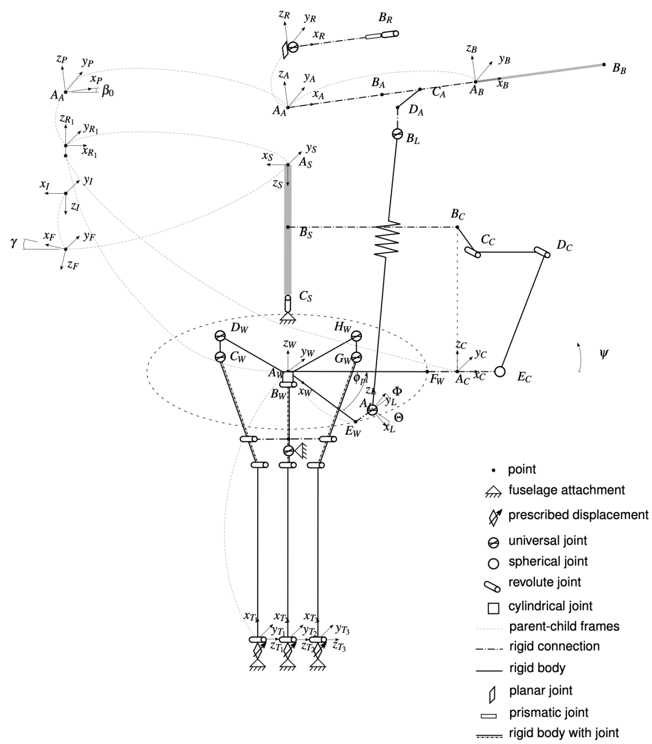

Figure 2: Illustration of the multibody dynamics model of the Bo 105 rotor in DYMORE. Note that the illustration is not to scale.

The NN model is particularly lucrative given its potential in real-time noise prediction, which can instantly output the prediction results. This study proposes an NN to rapidly predict the rotor rotational noise of the full-scale helicopter while promising high accuracy. The dataset used for the training model was obtained from a traditional FW-H equation-based solver, PSU-WOPWOP. This investigation will systematically quantify this method's accuracy in predicting rotor rotational noise at arbitrary spatial locations at different flight conditions and characterizing how noise propagates in space. This study will investigate the characterization of noise concerning the input variables.

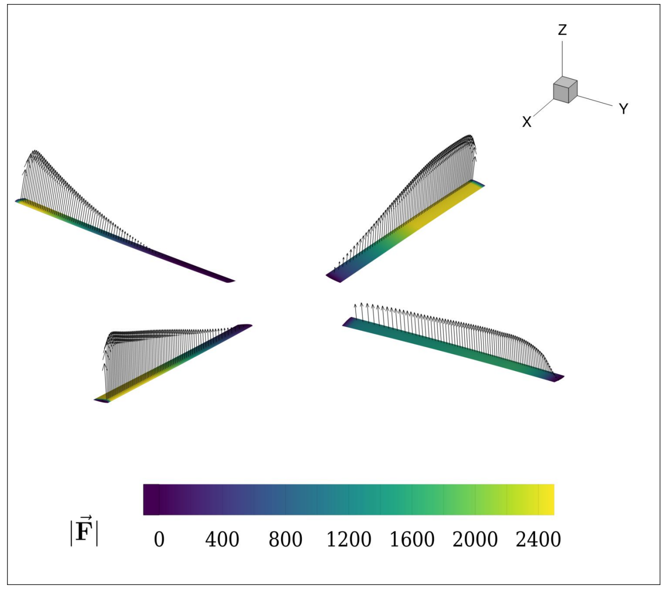

Figure 3: Illustration of aerodynamic loading based on lifting-line theory.

MODELLING APPROACH

The current investigation used a rotor comprehensive analysis tool, DYMORE, to calculate the rotor blade aerodynamics information. The rotor used in this study is a full-scale Bo 105 helicopter, which is shown in Fig. 1 and its rotor details are given in Table 1. Blade aerodynamics information is the noise source information in acoustic analysis code, PSU-WOPWOP, and is used to solve the Ffowcs Williams-Hawkings analogy to calculate the noise. PSU-WOPWOP is used to generate a dataset to train the neural network model.

Rotor comprehensive analysis tool - DYMORE

DYMORE is a finite element based tool for the analysis of nonlinear flexible multibody systems and allows representation of complex topologies with high fidelity, which is proposed in (Ref. 17). It implements a multibody dynamics approach to the modeling of nonlinear elastic multibody systems and is widely used as a fundamental design tool in many areas of mechanical engineering. This approach models the complex configuration of the helicopter rotor system through the assembly of basic components chosen from an extensive library of elements that includes rigid and deformable bodies such as beams, cables, shells, etc, and different joints and constraint modelling abilities as well as numerous joint elements. Physical and geometric properties can be defined for all joints as well as bodies connecting the joints.

In this study, DYMORE is used to model the multibody dynamics model of the Bo 105 helicopter rotor. Fig. 2 illustrates the topology of the Bo 105 main rotor system used in the current study together with relevant reference frames. Note that the figure is not to scale in order to show the rotor drive train in sufficient detail. An elastic fuselage is not modeled. Therefore, the end of the shaft is rigidly fixed with respect to an inertial frame. The rotor blade structure is modeled as a one dimensional beam using a geometrically exact formulation. The finite-element discretization of the rotor blade consists of 14 elements and a linear shape function distributed equally throughout the blade.

The rotor aerodynamics solution is obtained by separate blade and wake aerodynamics models - inner and outer problem approach (Ref. 18). The blade aerodynamics model in DYMORE is based on lifting-line theory, which can be found in Section 2, Chapter 5.3 of (Ref. 19). The detailed explanation for the blade aerodynamics model used in this study can be found in (Ref. 20). Briefly speaking, the rotor blade is considered a 1-D beam and discretized along the span direction. Fig. 3 illustrates the aerodynamic loading diagram calculated based on lifting-line theory.

The rotor wake effects were separately incorporated using the wake-induced velocity on the blade sections using the viscous vortex particle method (VVPM). VVPM solves the incompressible Navier-Stokes equations in a vorticity-velocity form with a grid-free Lagrangian frame representation. The domain of investigation of fluid flow around a body of interest is also limited to the region where vorticity in the flow, represented using particles, dominates. As a consequence, this methodology gained traction as an alternative to grid-based computational fluid dynamic techniques. A detailed mathematical explanation of VVPM can be found in (Ref. 20).

FW-H equation solver - PSU-WOPWOP

The rotor noise prediction code PSU-WOPWOP, was developed at Penn State University by Prof. Kenneth Brentner and his students (Ref. 9), was used to generate the noise dataset in the present study.

Theoretically, the Ffowcs Williams-Hawkings equation (Eq. 1) solves the reformulated continuity and Navier-Stokes equations using generalized functions for arbitrarily moving surfaces to determine the acoustic pressure generated by them (Ref. 10). This formulation categorizes sound sources into three types: monopole, dipole, and quadrupole.

$$\frac{1}{c^2}\frac{\partial^2 p'}{\partial t^2} - \nabla^2 p' = \underbrace{\frac{\partial}{\partial t}\left[\rho_o v_n \delta(f)\right]}_{\text{monopole source term}} - \underbrace{\frac{\partial}{\partial x_i}\left[l_i \delta(f)\right]}_{\text{dipole source term}} + \underbrace{\frac{\bar{\partial}^2}{\partial x_i x_j}\left[T_{ij} H(f)\right]}_{\text{quadrupole source term}} \tag{1}$$

Since the FW-H equation is essentially a rearrangement of the Navier-Stokes equations, solving it over the flow domain is as challenging as solving the Navier-Stokes equations themselves. However, it is formulated in generalized function space, making it valid in unbounded space. This characteristic allows it to be solved using the free-space Green's function. Farassat proposed an integral solution in time and space in (Ref. 8), referred to as Farassat's 1A (Eq. 2).

$$\begin{aligned} 4\pi p'(\mathbf{x},t) = & \underbrace{\int_{f=0} \left[\frac{\rho_o(\dot{v}_n + v_n)}{r(1-M_r)^2}\right]_\tau + \left[\frac{\rho_o v_n \left(r\dot{M}_r + c\left(M_r - M^2\right)\right)}{r^2(1-M_r)^3}\right]_\tau dS}_{\text{monopole source term (thickness noise)}} \\ & + \underbrace{\frac{1}{c}\int_{f=0}\left[\frac{i_r}{r(1-M_r)^2}\right] + \left[\frac{l_r - l_M}{r^2(1-M_r)^2}\right] + \left[\frac{l_r\left(r\dot{M}_r + c\left(M_r - M^2\right)\right)}{r^2(1-M_r)^3}\right]_\tau dS}_{\text{dipole source term (loading noise)}} \end{aligned} \tag{2}$$

Here, an integration is performed over the impermeable surface that perturbs the flow, specifically the rotor blade, by evaluating the relevant quantities at source time τ. The subscripts n and r correspond to the vector directions normal to the surface f (i.e., the blade surface over which the surface integral is evaluated) and the radial direction between the surface grid cell and the observer, respectively. The parameters ρ_0 and c refer to the quiescent flow properties: flow density and the speed of sound. v represents the surface grid velocity, M denotes the Mach number, and l is the loading force acting on the fluid due to the surface element dS.

However, Farassat's Formulation 1A does not take the elastic deformation of small arbitrarily moving surfaces. Farassat's Formulation 1A - Flexible (Eq. 3) is adapted from Farassat's Formulation 1A and includes the effect of elastic deformation of the moving surface and is used in this study. The theory of Farassat's Formulation 1A and 1A - Flexible is explained in detail and clearly in Chapter 2 of (Ref. 21).

$$\begin{aligned} 4\pi p'(\mathbf{x},t) = & \underbrace{\int_\Omega \left[J\frac{\rho_0(\dot{v}_n + v_n)}{r|1-M_r|^2}\right] + \left[\frac{\rho_0 v_n}{r|1-M_r|^2}\right] - \left[J\frac{\rho_0 v_n\left[r\dot{M}_r + c\left(M_r - M^2\right)\right]}{r^2|1-M_r|^3}\dot{J}\right]_{\text{ret}} du_1 du_2}_{\text{monopole source term (thickness noise)}} \\ & \underbrace{\frac{1}{c}\int_\Omega \left[J\frac{\dot{L}_r}{r|1-M_r|^2}\right] + \left[J\frac{-cL_M + v_r L_r}{r^2|1-M_r|^2}\right] + \left[\dot{J}\frac{L_r}{r|1-M_r|^2}\right] + \left[J\frac{L_r c M^2 - r L_r \dot{M}_r}{r^2|1-M_r|^3}\right]_{\text{ret}} du_1 du_2}_{\text{dipole source term (loading noise)}} \end{aligned} \tag{3}$$

In Eq. 3, the total acoustic pressure perturbation is ascribed to physically relevant attributes such as the lifting-surface geometry (thickness noise) and the blade airloads (loading noise). In the absence of high-speed impulsive noise, i.e., if the Mach number at any blade section is below 0.9 (Ref. 22), the quadrupole-like source term in Eq. 1 is usually dropped, and Eq. 3 can be used to predict rotor noise fairly accurately. For the maximum advanced ratio μ = 0.15 investigated in this study, the advancing blade tip Mach number does not exceed 0.74. This procedure has become standard practice for predicting rotor noise, particularly for helicopter main rotor noise, as it allows for the use of detailed blade geometry and blade airloads to predict rotor noise with reasonable accuracy.

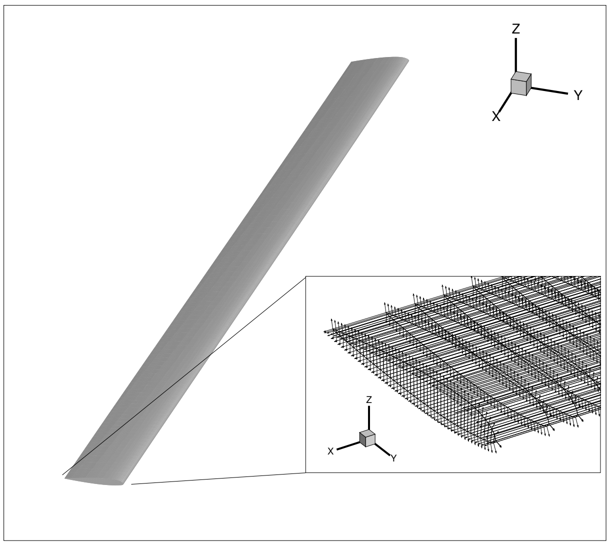

Figure 4: Bo 105 rotor blade surface discretization

Deep learning model

The current study uses a multilayer perceptron (MLP) as the deep learning model for quickly predicting noise. To predict helicopter rotor noise at arbitrary observer locations and different flight velocities within the design space, the spherical coordinates of observers—radius r_o, azimuth angle ϕ_o, elevation angle θ_o—and advanced ratio β are employed as input parameters to the MLP model. The perception of sound is the response to a physical stimulus to the ear. This stimulus is the unsteady sound pressure, which is reflected by the overall sound pressure level (OASPL). So, MLP predicts OASPL of the noise.

As shown in Fig. 5, the MLP consists of three parts: the input layer, hidden layers, and the output layer. In this study, the number of neurons in the hidden layers, batch size, and learning rate, these three hyperparameters were determined using a technique called grid search. Grid search, as illustrated in Fig. 6, is a hyperparameter tuning technique used to optimize machine learning models. It involves defining a set of hyperparameters to evaluate, performing an exhaustive search over all possible combinations, and using cross-validation to assess each combination's performance. The best-performing set of hyperparameters is then selected based on a predefined metric, which is the training loss in this study. The design of the grid search is shown in Table. 2.

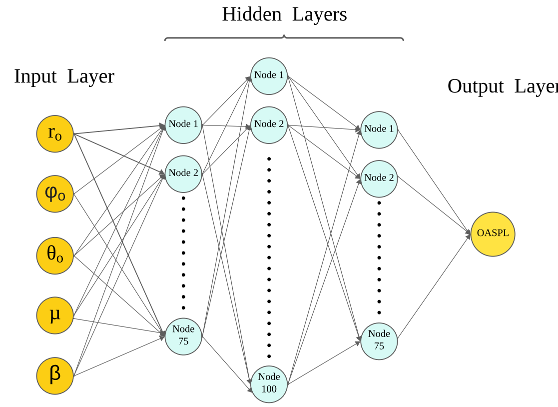

Figure 5: Deep learning model configuration.

The optimal hyperparameter combination is (75, 100, 75), the batch size is set as 32 and the learning rate is 0.005. The input layer has 5 neurons, corresponding to the five input parameters. The output layer has 1 neuron, representing the noise OASPL. The activation function is the ReLu function, which introduces non-linearity into the model, enabling it to learn and represent complex patterns in the data.

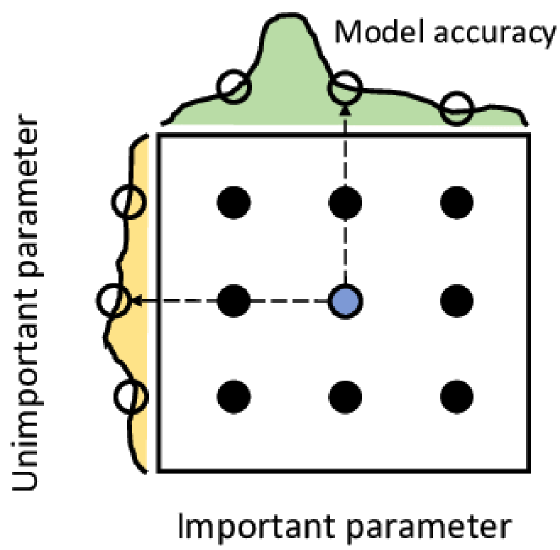

Figure 6: Illustration of grid search.

For instance, for hidden layer size, (75, 75) means two hidden layers with 75 neurons each. The batch size is multiples of 16 simply because it is compatible with the graphics processing unit (GPU) architecture.

In addition to hyperparameters, determining the appropriate number of epochs is crucial for a deep learning model's ability to generalize from the training data. An epoch refers to a complete pass through the entire training dataset by the learning algorithm. During each epoch, the model processes all train-

Table 2: Hyperparameters range of grid search.

Hidden layer size	$(75,75),(100,100),(75,100),(100,75),$ $(50,100,50),(50,100,75),$ $(75,100,75),(100,100,100)$
Learning rate	$0.0001,0.0005,0.001,0.005,0.01,0.05$
Batch size	$16,32,64$

ing examples once, allowing it to adjust its weights based on the computed loss. However, using a large number of epochs can lead to overfitting, where the model becomes too tailored to the training set, thus failing to generalize effectively to new data.

Table 3: Design space of MLP model.

μ	$0.10,0.11,0.12,0.13,0.14$
r_o	$10,12,14,16,18,20,30,40,50,60,80,100,$ $200,300,400,500,600,700,800,900$
ϕ_o	$0-2\pi$
θ_o	$0.5\pi-\pi$
β	$0,0.0467,0.0934,0.14$ rad

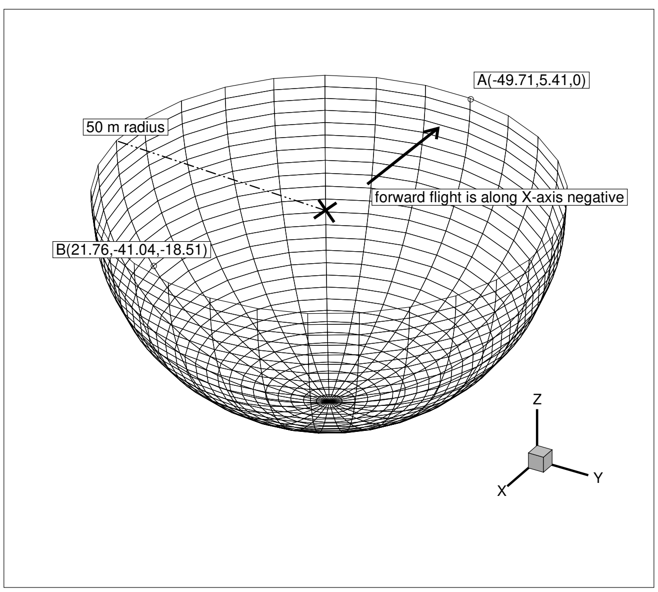

Figure 7: Observer distribution illustration

To address this issue, early stopping is often employed as a regularization technique. This method involves monitoring the model's performance on a validation set during training and halting the process when the validation loss reaches an appropriate threshold. This technique ensures the model retains its ability to generalize to unseen data, preventing the model from overfitting into the training dataset, and balancing training duration with model accuracy. In this case, the validation loss threshold is set to 0.1, which is accurate enough for noise prediction, with the maximum number of epochs set to 1000. The model training will cease once the validation loss falls below 0.1.

Dataset design

The spherical coordinates are based on the helicopter rotor, meaning the origin is the rotor hub. Additionally, one rotor operation parameter, the rotor shaft tilt angle θ, is also used as an input parameter. Thus, there are five input parameters in total. Table 3 details the design space.

For the observer radius r_o, sampling is more intensive in the near-field due to the increased complexity of near-field noise compared to far-field noise. Additionally, the near-field noise pattern exhibits rapid variation as the distance from the helicopter hub changes. Consequently, it is prudent to allocate more sampling points in the region close to the helicopter rotor.

The observer azimuth angle ϕ_o ranges from 0 to 2π, with 30 sampling points, while the observer elevation angle θ_o ranges from 0.5π to π, with 15 sampling points. This distribution of observers forms a hemisphere centered on the rotor hub and positioned beneath the rotor plane, as illustrated in Fig. 7. The total number of data points is calculated as $5\times20\times30\times15\times4=180,000$. These data are then randomly split, with 80% allocated to the training set and 20% to the validation set.

To address the varying scales of the five input parameters, data standardization is applied as a pre-processing technique. For instance, the maximum shaft tilt angle β is 0.14, while the minimum observer radial coordinate r_o is 10. The disparity in scales among these parameters can bias the dataset, complicating the neural network's ability to accurately identify correlations between input parameters and outputs. Larger-scale parameters tend to exert a more substantial influence on the network due to their magnitude, even though their actual impact on the output may not correspond proportionately. Consequently, a biased dataset hampers the neural network's capacity to discern the correct underlying relationships. Thus, data standardization is necessary to enhance both the speed and accuracy of neural network training.

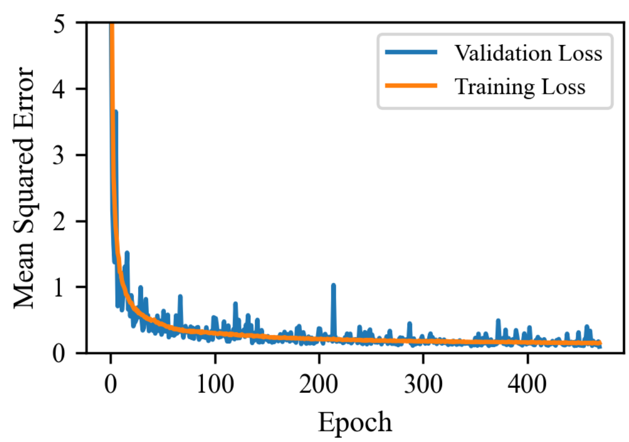

Figure 8: Convergence study of MLP model.

The data standardization process is governed by the equation presented in (4).

$$z = \frac{x - u}{s} \tag{4}$$

Here, u represents the mean of each input parameter, and s denotes the standard deviation. Post-standardization, all input parameters are normalized to the same scale, with a zero mean and a standard deviation of 1.

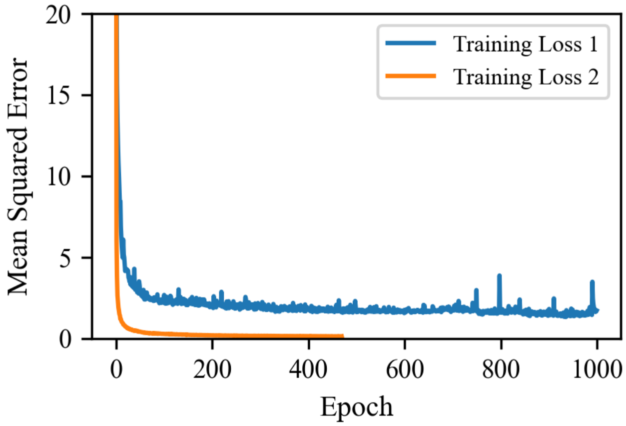

(a) Traing loss comparison.

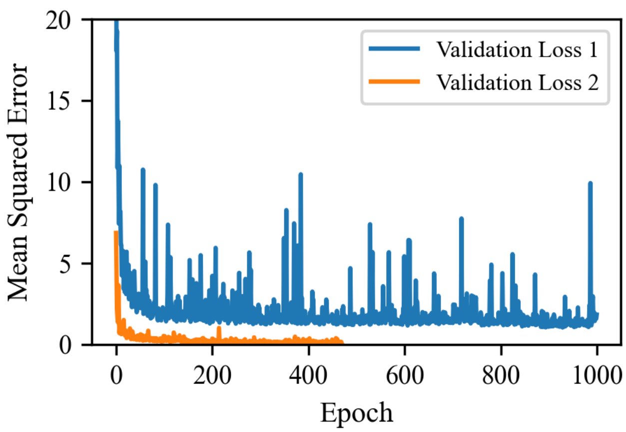

(b) Validation loss comparison.

Figure 9: MLP model convergence comparison: Without data standardization (Loss 1) and with data standardization (Loss 2).

RESULTS

This section presents the training results of the deep learning model and examines the impact of data standardization by comparing training outcomes with and without standardization. The distribution of noise prediction errors is then discussed, along with the average and maximum prediction errors. Finally, an analysis is conducted regarding the model's characterization in relation to five input parameters.

Training results

As mentioned in the deep learning model section , grid search was employed to determine the optimal hyperparameters of the MLP model, resulting in an optimal hidden layer configuration of (75, 100, 75).

Figure 8 illustrates the convergence study, where it is noteworthy that training was early stopped at epoch 483 when the validation loss reached the threshold of 0.01.

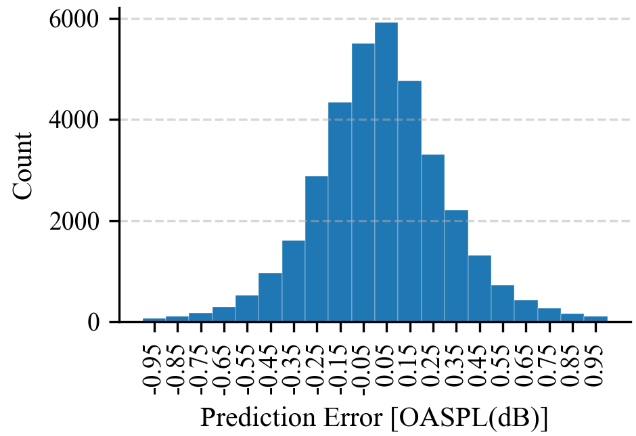

(a) Histogram of the noise prediction error in validation dataset.

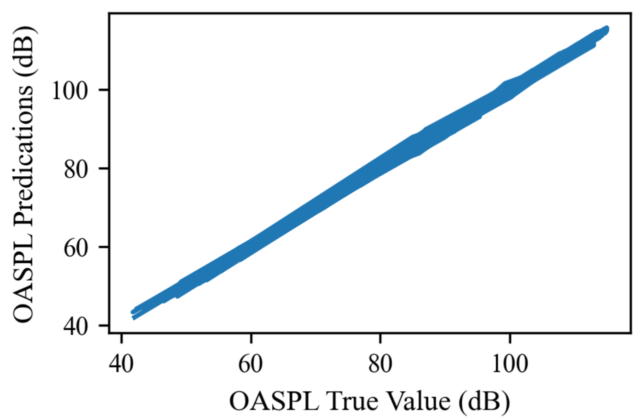

(b) Comparison between true noise OASPL and predicted noise OASPL.

Figure 10: Distribution of noise prediction error in validation dataset.

In this case, the MLP model converges very quickly and stably, indicating its ability to efficiently identify the mathematical relationships between input parameters. Data standardization plays a crucial role in achieving this rapid convergence. The original data is biased due to the significant differences in the scales of the input parameters. Standardization corrects this issue, making it easier for the MLP to identify correlations between the parameters.

Figure 9 presents a comparison of the MLP model's convergence with and without data standardization. The train-

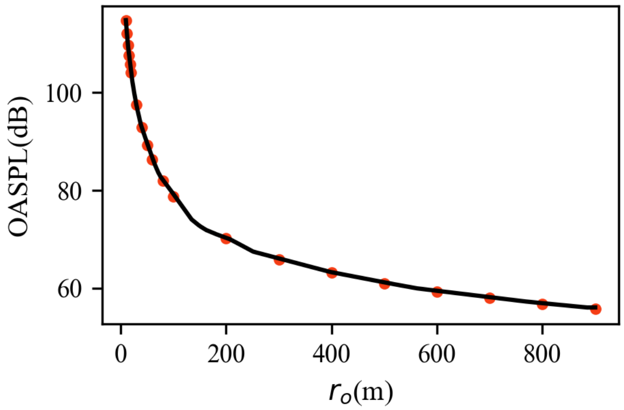

Figure 11: Observer radius r_o characterization by MLP model.

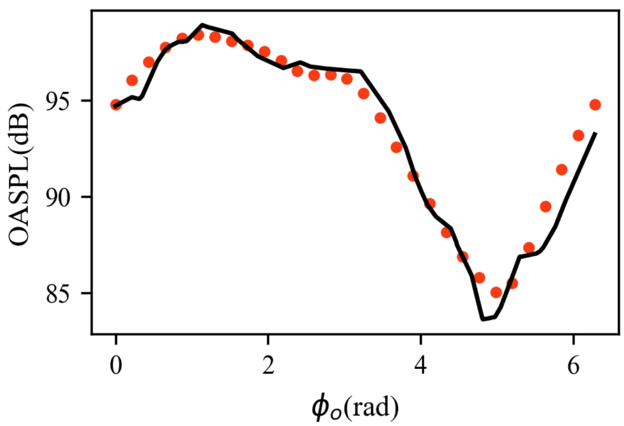

Figure 12: Observer azimuth angle ϕ_o characterization by MLP model.

ing process with standardized data reaches the validation loss threshold before hitting the maximum epoch number, whereas the training process with the original data fails to achieve the same low validation loss, even after reaching the maximum of 1,000 epochs. Hence, the MLP model trained with the standardized data in this study.

The maximum epoch number is 1,000 because, around this point, the validation loss begins to fluctuate significantly without further improvement, indicating that additional epochs will lead to overfitting rather than enhancing the model's generalization performance. In addition, when the MLP model trained with standardized data is used to predict a new, unseen dataset, this new dataset must also be standardized using the same standardization parameters.

Figure 10a shows the histogram of the noise prediction error in the validation dataset, with errors concentrated between -0.4 dB and 0.4 dB. The maximum and average validation errors are 2.939 dB and 0.225 dB, respectively. Figure 10b presents the comparison between the true noise OASPL and the predicted noise OASPL, where the validation errors are

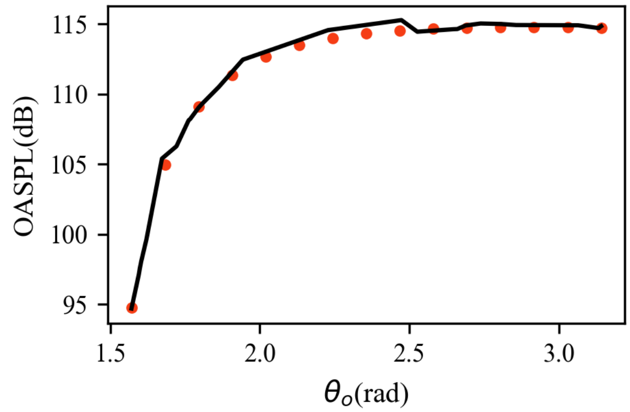

Figure 13: Observer elevation angle θ_o characterization by MLP model.

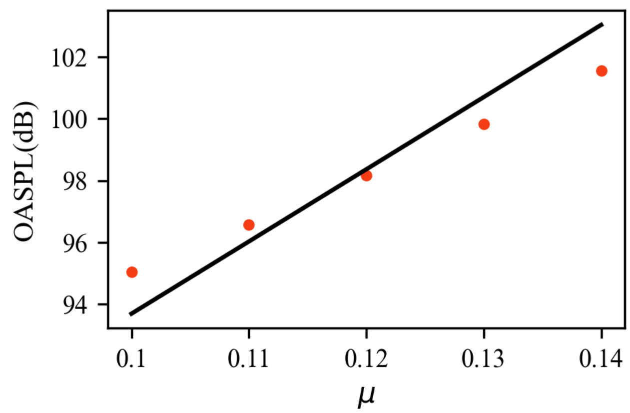

Figure 14: Advanced ratio μ characterization by MLP model.

uniformly distributed across the entire range.

Characterization

For parameter characterization, the base parameters are $r_o = 10$ m, $\phi_o = 0$, $\theta = 1.5708$ rad, $\mu = 0.10$, and $\beta = 0$. This means that during each characterization, the other four parameters remain fixed at these base values.

Figure 11 illustrates the variation in noise OASPL with changes in the observer radius r_o. The results clearly show that noise decay follows the $1/r^2$ rule in the near-field and transitions to the $1/r$ rule in the far-field. The MLP model successfully captures this relationship, demonstrating its effectiveness in modeling the spatial decay of noise with respect to the observer's distance from the source.

In Figure 12, the characterization of the observer azimuth angle ϕ_o is presented. The MLP model accurately reflects the variation in noise levels as the azimuth angle changes. For the observer elevation angle θ_o, as shown in Figure 13, the noise increases with the elevation angle. This trend is attributed to the dominance of loading noise over thickness noise in forward flight, which significantly influences the noise distribu-

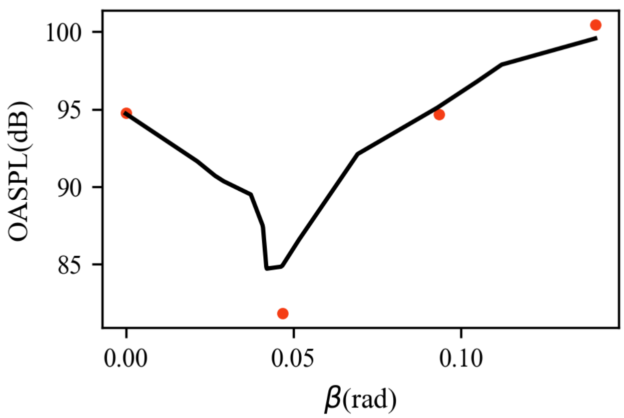

Figure 15: Rotor shaft tilt angle β characterization by MLP model.

tion outside the rotor plane. The MLP model captures this trend.

However, when characterizing the advanced ratio μ and rotor shaft tilt angle β, shown in Figures 14 and 15 respectively, the MLP model exhibits less precision in capturing the relationship between these parameters and noise variations. This discrepancy should be due to less sampling points of these parameters compared with the other three parameters.

CONCLUSIONS

In this study, a deep learning model—a three-hidden-layer MLP model—was applied to predict the noise generated by a full-scale Bo 105 rotor. The noise dataset used for training and validating the MLP model was generated using the FW-H solver PSU-WOPWOP, with the acoustic source derived from a rotor comprehensive tool, DYMORE. This dataset includes five input parameters: observer radius r_o, observer azimuth angle ϕ_o, observer elevation angle θ_o, advanced ratio μ, and rotor shaft tilt angle β. Given the deep learning model's capability to provide instant output, the study aims to quantify its accuracy in predicting noise OASPL for arbitrary observer locations in different flight speeds within the design space. Based on the results obtained, the following conclusion can be drawn:

1. The original data generated by PSU-WOPWOP needs to be standardized to ensure that all parameters have the same scale. With data standardization, both the training and validation losses are significantly reduced, and the MLP model converges much more quickly, which is shown in Fig. 9.

2. The MLP model can instantly provide output, with a maximum prediction error of 2.939 dB and an average prediction error of 0.225 dB on the validation set, which was not seen by the model during training. The histogram of validation error can be seen in Fig. 10a Additionally, the validation errors are uniformly distributed across the entire range, which is shown in Fig. 10b.

3. According to the parameter characterization results, the MLP model accurately captures the variations in the observer spatial coordinates (r_o, ϕ_o, θ_o), as shown in Figures 11, 12, and 13. However, as depicted in Figures 14 and 15, the MLP model's performance is slightly less accurate for the advanced ratio and rotor shaft tilt angle. This reduced accuracy is likely due to the fewer sampling points available for these two parameters.

Author contact:

Guowei Zhang guowei.zhang@tum.de,

Ilkay Yavrucuk ilkay.yavrucuk@tum.de

REFERENCES

1. Christelle Al Haddad, Emmanouil Chaniotakis, Anna Straubinger, Kay Plötner, and Constantinos Antoniou. Factors affecting the adoption and use of urban air mobility. *Transportation research part A: policy and practice*, 132:696–712, 2020.

2. Tiago Bacelar, João Madeiras, Rui Melicio, Carlos Cardeira, and Paulo Oliveira. On-board implementation and experimental validation of collaborative transportation of loads with multiple uavs. *Aerospace Science and Technology*, 107:106284, 2020.

3. Aleksandar Bauranov and Jasenka Rakas. Designing airspace for urban air mobility: A review of concepts and approaches. *Progress in Aerospace Sciences*, 125:100726, 2021.

4. Xice Xu, Yang Lu, Mengxue Shao, and Chunbo Lan. Fast prediction method for multirotor global tonal noise based on acoustic modal analysis. *Mechanical Systems and Signal Processing*, 183:109620, 2023.

5. CR Cox and RR Lynn. A study of the origin and means of reducing helicopter noise. *Bell Helicopter Co., USATCREC Technical Report*, pages 62–73, 1962.

6. Marc C Jacob, Didier Dragna, Adrien Cahuzac, Jérôme Boudet, and Ph Blanc-Benon. Toward hybrid caa with ground effects. *International Journal of Aeroacoustics*, 13(3-4):235–259, 2014.

7. BA Singer, DP Lockard, and GM Lilley. Hybrid acoustic predictions. *Computers & Mathematics with Applications*, 46(4):647–669, 2003.

8. Fereidoun Farassat. Derivation of formulations 1 and 1a of farassat. Technical report, 2007.

9. Kenneth S Brentner, Guillaume A Bres, Guillaume Perez, and Henry E Jones. Maneuvering rotorcraft noise prediction: A new code for a new problem. In *Ahs aerodynamics, acoustics and test evaluation specialist meeting*, 2002.

10. John E Ffowcs Williams and David L Hawkings. Sound generation by turbulence and surfaces in arbitrary motion. *Philosophical Transactions of the Royal Society of London. Series A, Mathematical and Physical Sciences*, 264(1151):321–342, 1969.

11. Donald B Hanson. Near-field frequency-domain theory for propeller noise. *AIAA journal*, 23(4):499–504, 1985.

12. Xice Xu, Yang Lu, Jiaxin Lu, and Mengxue Shao. Modal analysis of the influence of freestream on global rotor noise. *Journal of Sound and Vibration*, 555:117715, 2023.

13. Antonio Alguacil, Michaël Bauerheim, Marc C Jacob, and Stéphane Moreau. Predicting the propagation of acoustic waves using deep convolutional neural networks. *Journal of Sound and Vibration*, 512:116285, 2021.

14. Steffen Wiewel, Byungsoo Kim, Vinicius C Azevedo, Barbara Solenthaler, and Nils Thuerey. Latent space subdivision: stable and controllable time predictions for fluid flow. In *Computer Graphics Forum*, volume 39, pages 15–25. Wiley Online Library, 2020.

15. Sicheng Li and Seongkyu Lee. A machine learning-based fast prediction of rotorcraft broadband noise. In *AIAA AVIATION 2020 FORUM*, page 2588, 2020.

16. Christopher S Thurman and James D Baeder. Blade-wake interaction noise for small hovering rotors, part i: Characterization study. *AIAA Journal*, 61(6):2552–2569, 2023.

17. O Bauchau. Dymore: a finite element based tool for the analysis of nonlinear flexible multibody systems. *Georgia Institute of Technology*, 2001.

18. Wayne Johnson. *Rotorcraft aeromechanics*, volume 36. Cambridge university press, 2013.

19. John Anderson. *EBOOK: Fundamentals of Aerodynamics (SI units)*. McGraw hill, 2011.

20. Sumeet Kumar, Juergen Rauleder, and Ilkay Yavrucuk. Towards active rotor analysis using viscous vortex particle method. 2023.

21. Chris C Hennes, Leonard V Lopes, Justin Shirey, Rui Cheng, James Erwin, Seongkyu Lee, Benjamin A Goldman, Mrunali Botre, Damaris R Zachos, Ze Feng Ted Gan, et al. Psu-wopwop 3.4. 5 user's guide. Technical report, Technical report, The Pennsylvania State University, 2022.

22. Harvey H Hubbard. *Aeroacoustics of flight vehicles: theory and practice*, volume 1. National Aeronautics and Space Administration, Office of Management . . . , 1991.